

# Calibration of a Finite Element Forward Model in Eddy Current Inspection.

**DOI:**
10.1109/JSEN.2022.3167253

**Document Version**
Accepted author manuscript

# Calibration of a Finite Element Forward Model in Eddy Current Inspection. [1]

Joel Hampton [2], Henok Tesfalem [2], Oliver Dorn [3], Adam Fletcher [2], Anthony Peyton [2], and Matthew Brown [4]

April 22, 2022

[1]This document is the result of the research project funded by the UK Engineering and Physical Science Research Council (grant number EP/L022125/1) and EDF Energy.

[2]J. Hampton, H. Tesfalem, A. Fletcher and A. Peyton are with the Department of Electrical and Electronic Engineering, University of Manchester, Manchester, M13 9PL, United Kingdom. Corresponding author email: joel.hampton@manchester.ac.uk

[3]O. Dorn is with the Department of Mathematics, University of Manchester, Manchester, M13 9PL, United Kingdom. Corresponding author email: oliver.dorn@manchester.ac.uk

[4]M. Brown is with EDF energy, Barnwood, Gloucester, GL4 3RS, United Kingdom.

**Abstract**

We report on the use of a novel constrained optimisation algorithm for calibrating the finite element model in an eddy current inspection application. An accurate finite element forward model is often important in such eddy current applications for training neural networks or as part of an iterative solver. However, the subject of calibration of the model has not received much attention in the literature to date. We consider a multi-frequency, eddy current depth profiling application, which is important for non-destructive testing in the nuclear industry. In the optimisation algorithm, we use a Levenberg-Marquardt algorithm and a bisection search to ensure constraints are satisfied, coupled with a truncated Gradient and Hessian method. We calibrate two types of finite element models, one using a filament representation for the coils and the other using a full 3D approach. The results show the feasibility of using the constrained non-linear optimisation algorithm for tuning the finite element model parameters. The mean signal-noise ratio after tuning on a truncated spectrum was 29.47 dB for the 3D model and 28.96 dB for the filament; in contrast the mean SNR using the measured coil parameters was 1.48 dB and 4.98 dB for the two uncalibrated models, respectively. The results show that a filament model is competitive with a 3D model of the coils (within the nuclear graphite application); therefore, a computationally faster filament model can be used with minimal effect on accuracy.

# 1 Introduction

Calibration of a measurement system is important when some material property or value is to be evaluated and quantified. Calibration typically involves applying known inputs and adjusting system parameters to minimize the measurement error. In the case of eddy current inspection, the system may be dependent on a forward model, typically a finite element model (FEM). An accurate forward model is often important in such eddy current applications for training neural networks or as part of an iterative solver. However, the subject of calibration of the forward model has not received much attention in the literature to date.

We consider the application of multi-frequency, eddy current depth profiling of electrical conductivity on nuclear graphite. The electrical conductivity can be mapped to volumetric density and is important for further understanding of degradation processes and potentially controlling reactivity. Imaging the core using eddy current data has been previously demonstrated in work such as [1] and [2]. Calibration of the forward model is important in other tomographic imaging modalities and applications; for example, in medical imaging of the lungs [3].

In eddy current or electromagnetic inspection, optimisation techniques can be used to minimise the error between a FEM simulation and the physical measurements [1][4][5][6][7]. Prior to employing a FEM in an optimisation algorithm, the parameters within the FEM need to be calibrated, such that the FEM accurately encapsulates the physical system. Further, machine learning methods are becoming increasingly popular for image reconstruction, wherein large amounts of training data are required. This training data can be acquired experimentally, numerically or analytically. If a numeric or analytic model is to be used to produce synthetic training data, then good agreement between model and simulated data is essential [8][9][10].

Calibration procedures vary in eddy current inspection, a common approach is to obtain a series of reference measurements for materials of known characteristics. Properties of the measurements can then be inferred from the reference samples; for example, in determining the presence of a notch [11]. In methods which require forward models, the calibration stage must minimise modelling inaccuracies. In electromagnetic inspection of the graphite core, calibration procedures for tuning forward models have included various techniques: varying coil diameter and finding the diameter corresponding to the best model agreement[12] or mapping the FEM and physical system

using a transfer function approach [13] or a mixture of both. In [14], the forward model was calibrated by first accounting for losses and stray capacitance between coil windings and then minimising the difference between the measured and simulated responses by solving a least squares problem via the update of model lift off; in this paper we similarly calibrate by solving a least squares problem but on a larger scale as there are 11 coil parameters which are to be optimised.

The aim of this paper is to present a rigorous methodology for FEM calibration and to show how this information can be used in model selection and in refining the measurement (such as the frequency range). We present a novel algorithm for solving a constrained optimisation problem, using a trust region strategy. Although the framework in this paper is in a particular eddy current non-destructive testing application of importance to the nuclear industry, the approach could be more generally applied. Therefore, it is hoped it will be useful to those of a wider audience who wish to calibrate a numeric or analytic forward model in order to reconstruct material properties or behaviour.

# 2 Theory

In inductance spectroscopy the complex inductance variable, $\mathfrak{M}(f, \vec{\eta}; \vec{\rho})$, is sampled at a number of different frequencies, $f$; where $\vec{\rho}$ is any electromagnetic material variable, such as permeability ($\mu$), permittivity ($\epsilon$) or conductivity ($\sigma$), and $\vec{\eta}$ contains the coil parameters.

In this paper we are concerned only with imaging electrical conductivity; therefore, in the calibration procedure, a material with an *a priori* known electrical conductivity is used. To simplify the modelling, we use a known block of material with a homogeneous conductivity. The aim is to determine $\vec{\eta}$ from a set of inductance measurements, $\vec{\mathfrak{M}}$, such that $\mathfrak{M}_i \in \mathfrak{M}(f_i, \sigma; \vec{\eta})$ — in this calibration framework, the conductivity variable is a scalar and is fixed, and the inductance measurement is a function of the coil parameters.

To determine the coil parameters we find the minimum of an objective function, $f(\vec{\eta})$, subject to some constraints — this is given in eq. 1, where $l$ is the lower limit, $u$ is the upper limit, $j$ is the index and $I$ is the set of indices corresponding to the constrained variables. The variables in violation are referred to as belonging to the set $V$, where $\left\{ l^j > \eta^j \vee \eta^j > u^j, \quad j \in V. \right.$

$$\min f(\vec{\eta}) \text{ , s.t. } \Big\{ l^j \leq \eta^j \leq u^j, \quad j \in I. \tag{1}$$

Writing $\vec{\eta}$ as some step $\vec{p}$ from a point $\vec{\eta}_k$, we can define $\vec{\eta} = \vec{\eta}_k + \vec{p}$. This can be used to define the recursive relation $\vec{\eta}_{k+1} = \vec{\eta}_k + \vec{p}$; updates to $\vec{\eta}$ are chosen such that the next iterate is closer to a minimum. There are numerous methods for choosing $\vec{p}$, most of which are derived from the second order Taylor series approximation of $f(\vec{\eta})$ given by eq. 2, where at some point $\vec{\eta}_k$ $\nabla_{\vec{\eta}} f(\vec{\eta}_k)$ is the gradient, $\boldsymbol{H}_f(\vec{\eta}_k)$ is the Hessian matrix and $q(\vec{p})$ is the quadratic model approximation.

$$f(\vec{\eta}_k + \vec{p}) \approx q(\vec{p}) = f(\vec{\eta}_k) + \nabla_{\vec{\eta}} f(\vec{\eta}_k)^T \vec{p} + \frac{1}{2} \vec{p}^T \boldsymbol{H}_f(\vec{\eta}_k) \vec{p} \tag{2}$$

The function to be minimised is the least squares formulation, given by eq. 3, where $\vec{r}(\vec{\eta})$ is the difference between the measured and simulated data.

$$f(\vec{\eta}) = \frac{1}{2} \left\| \vec{r}(\vec{\eta}) \right\|_2^2 \tag{3}$$

In this work, the measurand is a complex inductance measurement. This measurement could be the differential inductance of a gradiometer coil or it could be the mutual inductance spectrum of a single transmit-receive pair. In either case, the real and imaginary parts of the complex measurement are concatenated. For example, using a single transmit-receive pair inductance spectrum as the measurement, the variable $\vec{r}(\vec{\eta})$ would be the difference between the real and imaginary parts of the actual, $\vec{\mathfrak{M}}_t(\vec{\eta}_t)$, and simulated, $\vec{\mathfrak{M}}_s(\vec{\eta})$, inductance measurements, given by eq. 4, where $\vec{\eta}_t$ is the desired true solution.

$$\vec{r}(\vec{\eta}) = \begin{bmatrix} \Re\{\vec{\mathfrak{M}}_s(\vec{\eta}) - \vec{\mathfrak{M}}_t(\vec{\eta}_t)\} \\ \Im\{\vec{\mathfrak{M}}_s(\vec{\eta}) - \vec{\mathfrak{M}}_t(\vec{\eta}_t)\ \} \end{bmatrix} \tag{4}$$

The gradient of eq. 3 is given by eq. 5 and the Hessian approximated as eq. 6, where $\boldsymbol{J}$ is the Jacobian matrix.

$$\nabla_{\vec{\eta}} f(\vec{\eta}_k) = \boldsymbol{J}_k^T \vec{r}(\vec{\eta}_k) \tag{5}$$

$$\boldsymbol{H}_f(\vec{\eta}_k) \approx \boldsymbol{J}_k^T \boldsymbol{J}_k \tag{6}$$

To solve eq. 3 we used the Levenberg-Marquardt (LM) direction with scaling. Alternatives include the Broyden–Fletcher–Goldfarb–Shanno, NL2SOL and conjugate gradient algorithms; we opt for a trust region strategy because it

has been previously shown to yield good results in this modality for depth profiling electrical conductivity [15]. The LM algorithm is a trust region method where a constraint region is applied around the current iterate. This constraint region is chosen such that a quadratic approximation accurately represents the actual function to be minimised. The LM search direction is given by eq. 7. The damping matrix, $\boldsymbol{D}$, re-scales the problem [16]; an alternative problem can be solved by defining $\boldsymbol{D}\vec{p} = \vec{\omega}$, or equivalently $\vec{p} = \boldsymbol{S}\vec{\omega}$, where typically the choice of the matrix $\boldsymbol{D}$ is to scale the components of $\vec{p}$ in order to create approximately equal sensitivities across the component parts of $\vec{\omega}$. A heuristic choice for the matrix $\boldsymbol{D}$ is to use the diagonal values of the Hessian, such that $\boldsymbol{D}^T\boldsymbol{D} = diag\{\boldsymbol{H}_f(\vec{\sigma}_k)\}$ [17][18]. The damping parameter $\gamma$ implicitly determines the size of the constraint region. For further details see [18][19].

$$\vec{p} = -(\boldsymbol{J}_k^T\boldsymbol{J}_k + \gamma\boldsymbol{D}^T\boldsymbol{D})^{-1}(\boldsymbol{J}_k^T\vec{r}(\vec{\eta}_k)) \tag{7}$$

This search direction can be considered the solution to the regularised linear problem in eq. 8.

$$\vec{p} = \text{argmin}_{\vec{p}}(\frac{1}{2}\left\|\boldsymbol{J}_k\vec{p} + \vec{r}(\vec{\eta}_k)\right\|_2^2 + \frac{\gamma}{2}\|\boldsymbol{D}\vec{p}\|_2^2) \tag{8}$$

The size of the constraint region is modified depending on the quadratic model agreement with the objective function. This agreement is quantified by the gain ratio, given in eq. 9. If the quadratic model is accurate then $\rho \approx 1$ and the step towards the solution of $\text{argmin}_{\vec{p}}(q(\vec{p}))$ in the constrained region is trusted to be the step towards a minimum of $f(\vec{\eta})$; otherwise the constraint region can altered until there is a satisfactory $\rho$.

$$\rho \coloneqq \frac{f(\vec{\eta}_k + \vec{p}) - f(\vec{\eta}_k)}{q(\vec{p}) - q(0)} \tag{9}$$

The coil parameters must satisfy a number of constraints, the most obvious is the lift off — a negative lift off is not defined. Further examples include: the number of turns, the coil dimensions and the sequence of the coils. To enforce the constraints we could use regularisation techniques and apply a penalty function; however, this is not sufficient for constraints such as lift off, where no there is no tolerance for a constraint violation.

There are many constrained non-linear optimisation algorithms available, such as the gradient projection, barrier, penalty and augmented Lagrangian

methods [20][21]. Common approaches linearise the constraints and use linear or quadratic programming algorithms to solve the problem (using Lagrange multipliers) [22]. In depth analysis constrained optimisation can be found in[20][23].

Here, we use the trust region algorithm to naturally constrain the step, by finding the $\gamma$ that results in all the coil parameters being within the feasible set described by the constraints. However, if a variable is on or outside of some feasible boundary and the current step direction wishes to move it to the unfeasible set, then potentially $\gamma \to \infty$ — this would be catastrophic because no other variable can move. Instead, the variables in violation of some constraint are fixed and a reduced gradient and Hessian computed — a sub-problem is solved. This method uses Lagrange multipliers naturally present in trust region algorithms to select the best direction within the feasible set, corresponding to the free variables — a test for $\rho$ is performed to check the quadratic model is sufficient. In this formulation the damping term in eq. 8 is not necessarily a scalar quantity, but a matrix, such that the penalty becomes $\frac{1}{2}\|\boldsymbol{\Gamma}\boldsymbol{D}\vec{p}\|_2^2$, where $\boldsymbol{\Gamma}$ is a diagonal matrix containing the individual damping terms of the search direction. Any point with a constraint violation can then be considered to have $\gamma^j = \infty$. Therefore, this approach is similar to the interior-point trust region algorithm in [26], where modifications are made to the constraint region defined by $\boldsymbol{D}$.

# 3 Methodology

## 3.1 Application

In the actual, reactor application, the eddy current inspection tool contains the sensor coil and is moved up and down a channel by a hoist — this can be seen in fig. 1. The sensor coil is connected to the measurement device via an, approximately, 60 m long umbilical cable. Prior to deployment, the inspection tool is placed within a calibration block of known electrical properties. Unfortunately, this calibration data was not available for this experimental study and hence the use of flat graphite blocks, which were available with three different electrical conductivities.

It is prudent to use a variety of calibration blocks with different conductivities, such that the calibration error would be, ideally, conductivity invariant. We use three blocks that have low conductivity (LC), medium conductivity

(MC) and high conductivity (HC), where high and low are respective to the nuclear graphite application. The conductivity of the calibration bricks was physically measured using a four point probe [27], where we took 100 measurements of each brick (from all faces) and computed the truncated mean to eliminate outliers — we eliminated the top and bottom 10%. The conductivities determined were 11.0 kS/m, 39.6 kS/m and 85.3 kS/m.


Figure 1: The application considered in this paper: the eddy current inspection of the nuclear moderator channels within advanced gas-cooled reactors.

## 3.2 Complex Coil Geometry and parameters

The sensor coil considered is shown in fig. 2. We calibrate and compare two FEMs of the coil array to be used for reconstructing the electrical conductivity distribution of a material. The first type of coil model is a filament model and the second a full 3D coil model.

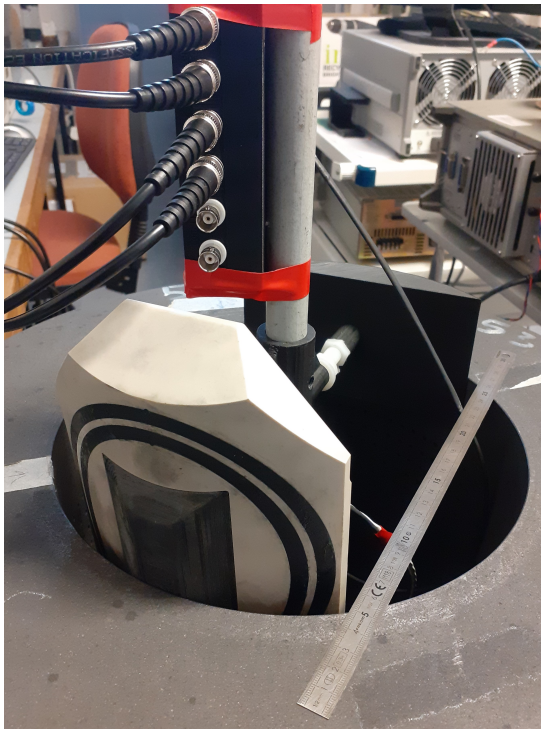

Figure 2: The sensor coil inside a graphite channel of the type used in the nuclear industry, with a ruler for perspective.

In the filament model, we approximate each receive and transmit coil with a wire filament, which has no cross section. This is an abstraction of the true coil in which the coil is modelled as resistively lossless. Within the filament model, the total voltage across a coil can be found by integrating the flux penetrating the filament and multiplying by the number of turns, assuming the flux through each coil is the same. However, the field is spatially varying and the amount of flux penetrating each turn of the physical coil is not necessarily uniform. This could be improved through the use of more filaments, capturing the spatial variation of penetration. The use of a filament model is simplistic but results in faster computation times because the number of finite elements in modelling the coil is reduced. In contrast, the 3D model captures the variation in flux between turns. Therefore, this model is generally more accurate but has longer computation times.

The elliptical coils are defined using the parameters in fig. 3. The geometry of the gradiometer coil evolved from studies into asymmetric gradiometer

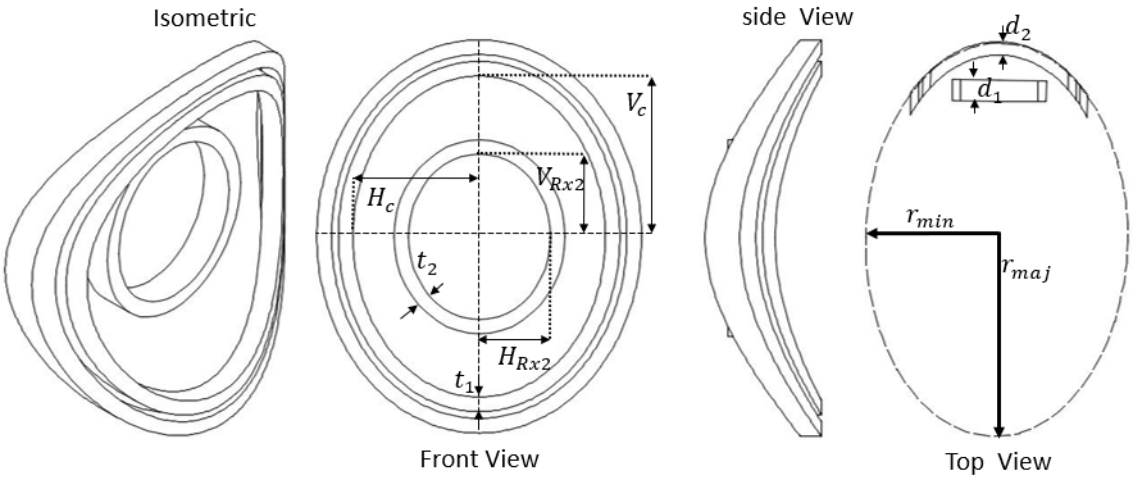


Figure 3: Engineering drawings of the sensor coil, characterised by the inset parameters. The top view shows how the curvature of the coil was defined, using an ellipse defined from an arbitrary origin.

designs in the nuclear application [24][25]; the geometry was chosen such that there was increased sensitivity at further distances from the sensor. The sequence of the coils is as follows: $\mathrm{Rx}_2$—Tx—$\mathrm{Rx}_1$, from smallest to largest. The large receive, $\mathrm{Rx}_1$, and transmit coil, Tx, lie on the same plane — the curvature of the surface is described by the major and minor radii of a 2D ellipse. In contrast, the small receive coil, $\mathrm{Rx}_2$, lies in a flat plane. All coils are elliptical in shape, as seen in the front view. In order to simplify the problem, the depth, $d$, and thickness, $t$, of $\mathrm{Rx}_2$, $\mathrm{Rx}_1$ and Tx are fixed in this work; we set the wire cross section so that the turns fit exactly according to the fixed depth and thickness. The fixed values are $d_1 = 14$ mm, $d_2 = 9$ mm, $t_1 = 6.35$ mm and $t_2 = 6.5$ mm. The coil dimensions are defined using the inner diameters and fixed thicknesses and depths. In this work, we do not update the diameters of $\mathrm{Rx}_1$ and Tx individually but instead define them off the inner diameters of the curved plane, $V_c$ and $H_c$ — the advantage of which is a reduced set of variables. For example, the horizontal inner diameter of $\mathrm{Rx}_1$ is $H_{Rx_1} = H_c + t_1 + 3.3 \times 10^{-3}$ and $H_{Tx} = H_c$ — we add 3.3 mm because this is the measured separation between the $\mathrm{Rx}_1$ and Tx coil. Similarly, we define a single lift off parameter, $L_c$, for the Tx—$\mathrm{Rx}_1$ pair. The smaller backing off coil has its own lift off parameter, $L_{Rx2}$. The number of turns, $T$, on each coil is treated individually.

## 3.3 Geometry Independence and the FEM

In calibrating the FEM to the actual measured data, we could tune the coil parameters such that geometry inaccuracies are implicitly reduced; ideally, the geometry would be well defined and the inaccuracies of the FEM due solely to the coil parameters and this is the assumption made in this work. We use a homogeneous cuboid block of graphite (see fig. 4) and this affords us with a basic geometry which can easily and accurately be defined, lowering the possibility of introducing geometrical errors. A template was used to fix the position of the coil for measurement consistency.

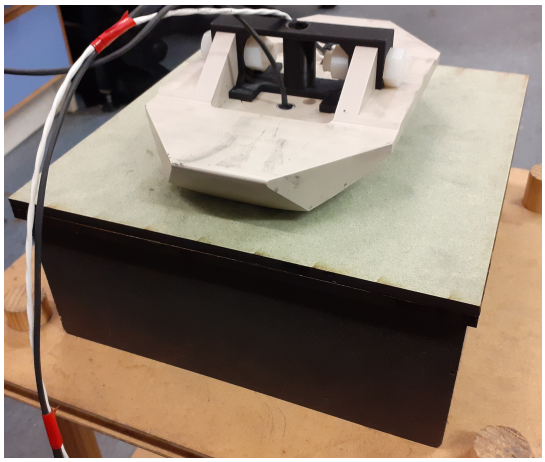

Figure 4: The setup used for calibration; a cuboid block of graphite with a template to fix the sensor position.

We use the symmetry of the problem to reduce computation times of the FEM, where the model can be split into one fourth and the relevant boundary conditions applied. The number of mesh elements for the 3D model was $\approx 130,000$ and for the filament $\approx 90,000$. The number of meshing elements and tessellation pattern changes with the sensor coil parameters, such as lift off, and this results in meshing noise which will be present in the sensitivity analysis — this is assumed to have minimal affect.

## 3.4 The Measurement

In the measurement used, we consider the mutual inductance of two receive coils, denoted by $\mathfrak{M}_{\mathrm{Rx}_1}$ and $\mathfrak{M}_{\mathrm{Rx}_2}$. The measurement made was the differen-

tial gradiometer response of the receiver coils in the presence of the conductive block and in air — given by eq. 10. We refer to this measurement as the differential mutual inductance (DMI). A perfectly balanced gradiometer would produce a response entirely due to material under inspection; when the gradiometer is balanced, the measurement in air is (ideally) equal to zero. However, gradiometer coils are generally not perfectly balanced, and therefore, the gradiometer response is differenced with air to eliminate common mode signals of the first order. Therefore, in the calibration procedure, we require two models: one of the gradiometer in air and the other the gradiometer with the graphite target.

$$m = (\mathfrak{M}^{\mathrm{c}}_{\mathrm{Rx}_1} - \mathfrak{M}^{\mathrm{c}}_{\mathrm{Rx}_2}) - (\mathfrak{M}^{\mathrm{air}}_{\mathrm{Rx}_1} - \mathfrak{M}^{\mathrm{air}}_{\mathrm{Rx}_2}) \tag{10}$$

This measurement was made at 10 different frequencies from from 10 Hz to 10 kHz. The agreement of the FEM with the physical measurements is quantified using the signal-noise ratio (SNR), given by eq. 11, where $m_s$ is the simulated measurement and $m_p$ the actual. After calibrating the measurement to this frequency range, we truncate the spectrum corresponding to the range of frequencies with the largest SNR. The measurements of the experimental data were made using a Solartron 1260 impedance analyser.

$$\psi(f_i) = 20 \times \log_{10}\left(\frac{\left|m_p(f_i)\right|}{\left|m_p(f_i) - m_s(f_i)\right|}\right) \tag{11}$$

## 3.5 Calibration Algorithm

If a predicted value $\eta_k^j + p^j$ had a constraint violation and the previous value $\eta_k^j$ was within the permissible boundary, then a bisection search was used to place $\eta_k^j + p^j$ on the boundary. If $\eta_k^j$ is already on some boundary and $\eta_k^j + p^j$ is in an impermissible set of values we cannot compute $\rho$. To proceed we omit the $j^{th}$ parameter from the step for the remainder of the iteration, by eliminating the variable from the gradient and Hessian; we then alter the damping parameter until the conditions on $\rho$ are satisfied, as normal. During the next iteration, any previously omitted parameters are re-introduced into the inversion and the full process above repeated. This freezing step ensures that other parameters can take on new values towards a minimum and, thus, the inversion can progress. In practice we have seen values that have been frozen later move from the boundary into the permissible space, as the algorithm navigates around some boundaries in the parameter space towards a

minimum. We refer to the set of variables that are within the feasible region as $\boldsymbol{F}_1$, those that are to be used in a bisection as $\boldsymbol{F}_2$ and $\boldsymbol{F}_3$ for those that are to be frozen — these three sets are disjoint and are formally written in eq. 12.

$$\begin{aligned}(l_j < \eta_k^j < u_j) \wedge (l_j \leq \eta_k^j + p^j \leq u_j), j \in \boldsymbol{F}_1 \\ (l_j < \eta_k^j < u_j) \wedge (\eta_k^j + p^j < l_j \vee \eta_k^j + p^j > u_j), j \in \boldsymbol{F}_2 \\ (\eta_k^j \leq l_j \vee \eta_k^j \geq u_j) \wedge (\eta_k^j + p^j \leq l_j \vee \eta_k^j + p^j \geq u_j), j \in \boldsymbol{F}_3\end{aligned} \tag{12}$$

The algorithm used for the bisection search is shown in algorithm 1; in this algorithm we complete a bisection search for the exponent because the sensitivity of the step to the damping parameter is in orders of magnitude, in this work. Within the bisection search, the objective is to find the $\gamma$ which results on parameters in violation being *close* to the boundary — it is numerically difficult to find a step landing exactly on the boundary. Due to this, we always select $\gamma = 10^{\text{low}}$, corresponding to a violation slightly beyond the boundary and into the impermissible region — this ensures that the $j \in \boldsymbol{F}_2$ will correctly be considered in the variables to be frozen in the next iteration. Alternative search algorithms could be used, such as the golden-section search which has a faster rate of convergence; however, the relative speedup in this work is negligible and so we opt for a bisection for its simplicity. The algorithm used in this work is shown in algorithm 2. In this algorithm, we first check to see which parameters are in $\boldsymbol{F}_2$. The first stage is to perform a bisection search to find the damping parameter corresponding to all the variables in violation moving close to or on the boundary — this stage is completed first because the indices in $\boldsymbol{F}_3$ may change with $\gamma$. We then freeze the variables in $\boldsymbol{F}_3$ by truncating the gradient and Hessian. We do not permit two bisection searches in a single iteration. The next stage is to compute $\rho$ and determine whether the quadratic model constraint region requires altering; an important stage is to check if a bisection search has been performed in the check for the over-constrained $\rho$ — this is required because we cannot lower the damping parameter as it will potentially place the variable further into the impermissible region. However, we are free to increase the damping parameter. For the damping parameter selection if $0.9 < \rho < 0.99$ or $1.01 < \rho < 1.1$ then the step was accepted, otherwise the region was contracted by increasing the damping parameter. The value of $\rho = 1$ was avoided as it is possible the constraint region is contracted

**Algorithm 1:** Bisection Search for the damping parameter exponent.

low $= \log_{10}(\gamma)$;
upper $= \log_{10}(\gamma) + 10$;
$i = 1$;
**for** $i <$ *bisection iterations* **do**
    mid $= (\text{low} + \text{upper})/2$ ;
    compute $\vec{p}(\gamma = 10^{\text{mid}})$;
    determine $\boldsymbol{F}_2$ with $\vec{p}(\gamma = 10^{\text{mid}})$;
    **if** $\boldsymbol{F}_2$ *is not empty* **then**
        low = mid;
    **else**
        upper = mid;
    **end**
    $\gamma = 10^{\text{low}}$;
    $i+ = 1$;
**end**
return $\gamma$;

to the point that the numerator and denominator tend to zero (producing numerical instability) and also affords us the ability to lower $\gamma$.

The objective function which was used is given by eq. 13. The quantity $\vec{r}^k(\vec{\eta})$ is the residual between the measured and simulated response of the $k^{th}$ calibration block and $n$ is the number of calibration blocks.

$$f = \frac{1}{2}\sum_{k=1}^{n}\left\|\vec{r}^k(\vec{\eta})\right\|_2^2 \tag{13}$$

The constraints used in this work are given in table 1. The constant $s$ is the minimum separation between $\text{Rx}_2$ and Tx and in this work is defined as the $\text{Rx}_2$ coil thickness plus some offset, where the offset used was 3 mm to ensure the coils can be suitably meshed. Additionally, the upper limit of $\text{Rx}_2$ is tied to the lower of Tx — if one is in violation then so is the other, enforcing the sequence of the coils. The lift off for each coil has no upper bound, but has a lower constraint of 3 mm, again to ensure the coils can be suitably meshed. The rest of the variables are constrained using the measured values with a 25% tolerance.

**Algorithm 2:** Computing the step direction

$\rho$ = Nan;
count = 1;
already bisected this iteration = False ;
**while** $\rho$ *does not satisfy constraints or count* $<$ *count limit* **do**
    compute $\vec{p}(\gamma)$;
    find $\boldsymbol{F}_2$ corresponding to $\vec{p}(\gamma)$;
    **if** $\boldsymbol{F}_2$ *is not empty and not already bisected this iteration* **then**
        $\gamma$ = compute bisection();
        already bisected this iteration = True;
        compute $\vec{p}(\gamma)$;
    find $\boldsymbol{F_3}$ corresponding to $\vec{p}(\gamma)$;
    **if** $\boldsymbol{F_3}$ *is not empty* **then**
        Truncate gradient and Hessian;
        Compute reduced step, $\vec{p}_r$, corresponding to indices in $\boldsymbol{F}_1 \cup \boldsymbol{F}_2$;
        Assemble full step $\vec{p}$ using $\vec{p}_r$, where $p^j = \begin{cases} 0, & j \in \boldsymbol{F}_3. \end{cases}$
    compute $\rho$ using step, gradient and Hessian corresponding to $\boldsymbol{F}_1 \cup \boldsymbol{F}_2$;
    **if** *over constrained* **then**
        **if** *already bisected this iteration* **then**
            $\vec{\eta}_{k+1} = \vec{\eta}_k + \vec{p}$;
            break;
        $\gamma = \gamma/2$;
    **else if** *Under-constrained* **then**
        $\gamma = \gamma \times 3$;
    **else if** *Not under-constrained or over constrained* **then**
        $\vec{\eta}_{k+1} = \vec{\eta}_k + \vec{p}$;
        break ;
    count += 1;
**end**
return;

Table 1: Constraints used in both models

| Parameter | $l^j$ | $u^j$ |
|---|---|---|
| $H_{Rx2}$ | 0.001 | $\frac{H_c+H_{Rx2}-s}{2}$ |
| $H_c$ | $\frac{H_c+H_{Rx2}+s}{2}$ | $\infty$ |
| $V_{Rx2}$ | 0.001 | $\frac{V_c+V_{Rx2}-s}{2}$ |
| $V_c$ | $\frac{V_c+V_{Rx2}+s}{2}$ | $\infty$ |
| $T_{Rx2}$ | 562.5 | 937.5 |
| $T_{Tx}$ | 75 | 125 |
| $T_{Rx1}$ | 112.5 | 187.5 |
| $L_{Rx2}$ | 0.003 | $\infty$ |
| $L_c$ | 0.003 | $\infty$ |
| $r_{min}$ | 0.1 | 0.12 |
| $r_{maj}$ | 0.1 | 0.12 |

To compute the Jacobian required for the gradient and Hessian, we use the perturbation method. In this approach the sensitivities are found using the forward difference method, given by eq. 14, where $f$ is defined from eq. 13. We report that for large values of $\gamma$ (decreasing constraint region radius), the gain ratio can become numerically erratic; this is because the scale of the constraint region radius approaches that of the perturbation. Because of this, we limited the value of the damping parameter to $\gamma < 10$.

$$\frac{\partial f(\vec{\eta})}{\partial \eta_k^j} \approx \frac{f(\eta_k^j + \Delta\eta_k^j) - f(\eta_k^j)}{\Delta\eta_k^j} \tag{14}$$

# 4 Results

The results presented correspond to five executions of the inversion algorithm described in the previous section. The measurements and SNR of the three calibration bricks, *prior* to optimisation, are shown in fig. 5 and table 2, respectively. Similarly, the measurements and SNR of the three calibration

bricks *post* optimisation are shown in fig. 6 and table 3, respectively. Comparing the FEMs prior to and post optimisation, we can see the validity of using a constrained optimisation algorithm for coil tuning.

Table 2: SNR of the 3D Model using the full spectrum — prior to optimisation

| frequency (Hz) | HC (dB) | MC (dB) | LC (dB) |
|---|---|---|---|
| 10 | -2.92 | -6.72 | -6.38 |
| 21.54 | 0.89 | -0.02 | 2.13 |
| 46.42 | 0.69 | -0.63 | -1.07 |
| 100 | 0.71 | -0.51 | -0.28 |
| 215.44 | 0.71 | -0.48 | -0.3 |
| 464.16 | 0.82 | -0.43 | -0.29 |
| 1000 | 1.25 | -0.29 | -0.23 |
| 2154.43 | 2.42 | 0.28 | -0.09 |
| 4641.59 | 3.86 | 1.71 | 0.43 |
| 10000 | 5.89 | 4.32 | 2.49 |

From fig. 6 we can see that the actual and simulated responses begin to clearly deviate at 215 Hz in the real part of the measurement of the low conductivity block; the low frequency error is expected because the measurement signal decreases in accordance with Faraday's law. Therefore, we truncate the spectrum's to 464 Hz - 10 kHz and repeat the optimisation procedure.

The results for the truncated spectrum are shown in table 4 for the 3D model. From table 3 and 4 we can see that there is not much improvement in the SNR's, thus, the lower frequency measurements were not necessarily limiting the convergence of the model parameters. Further, there may be coil modelling or measurement inaccuracies which are limiting convergence. The results for the truncated spectrum are shown in table 5 for the filament model. The mean SNR across the truncated spectrum and across the three calibration bricks is 29.43 dB for the 3D model and 28.27 dB for the filament.

Table 3: SNR of the 3D Model using the full spectrum — post optimisation

| frequency (Hz) | HC (dB) | MC (dB) | LC (dB) |
|---|---|---|---|
| 10 | 11.78 | -0.66 | -3.74 |
| 21.54 | 30.94 | 18.49 | 21.86 |
| 46.42 | 38.05 | 21.89 | 17.28 |
| 100 | 40.01 | 23.55 | 23.61 |
| 215.44 | 40.34 | 23.99 | 24.89 |
| 464.16 | 37.02 | 24.2 | 25.73 |
| 1000 | 33.89 | 24.13 | 26.45 |
| 2154.43 | 31.52 | 24.22 | 27.42 |
| 4641.59 | 31.78 | 25.6 | 31.23 |
| 10000 | 30.41 | 41.77 | 27.31 |

Finally, the initial measured and tuned coil model parameters are given in tables 6 and 7, where these are in descending order of relative change with respect to the measured parameters. The parameter which changed the most for both models is the lift off of the Tx and $Rx_1$ coils, where this commonality between two different models indicates possible measurement error in the lift-off; there are no other obvious trends between the two models.

From the data, it is clear that there is little difference between the two coil models, and therefore, the affects of the field geometry and coil losses were not the deciding factor between the two models. This could indicate that there is a common modelling error in both cases, or that there is systematic error in the measurement data. In this work a four point probe was used to measure the electrical conductivity of the blocks; therefore, the accuracy is potentially limited by the four point probe measurement. This would also go some way in explaining the asymptotic nature of the accuracy in both coil models. The assumptions made in this work are that the electrical conductivity distribution throughout the bricks is homogeneous — this is not necessarily a very good assumption, since there can be some spatial variations. To gain accuracy, it may be better to obtain bricks which have

Table 4: SNR of the 3D Model using the truncated spectrum — post optimisation

| frequency (Hz) | HC (dB) | MC (dB) | LC (dB) |
|---|---|---|---|
| 464.16 | 36.96 | 24.13 | 25.65 |
| 1000 | 33.68 | 24.05 | 26.35 |
| 2154.43 | 31.28 | 24.11 | 27.31 |
| 4641.59 | 31.54 | 25.45 | 31.04 |
| 10000 | 30.61 | 41.93 | 27.4 |

Table 5: SNR of the filament Model using the truncated spectrum — post optimisation

| frequency (Hz) | HC (dB) | MC (dB) | LC (dB) |
|---|---|---|---|
| 464.16 | 32.54 | 26.71 | 22.44 |
| 1000 | 30.28 | 26.08 | 22.84 |
| 2154.43 | 29.82 | 25.49 | 23.46 |
| 4641.59 | 31.59 | 27.64 | 26.01 |
| 10000 | 30.99 | 35.03 | 33.09 |

greater homogeneity or an electrical conductivity measurement more indicative of the brick average; the latter can be obtained by using a different four point geometry (greater distance between probes) and a larger number of measurements at different locations. Furthermore, accuracy may be limited by the finite element mesh. We repeated the optimisation with a finer mesh within the calibration block, using 111810 elements instead of the 40811 previously used; we report that optimisation on the truncated spectrum with the filament model achieved a mean SNR of 29.09 dB, where previously this was 28.27 dB. This indicates that the mesh size was not significantly limiting the accuracy, in this case.

Finally, the 3D model takes $\approx 89$ s to compute and the filament $\approx 54$ s — this is for the truncated spectrum where the computations were performed

Table 6: 3D Model Parameters

| Parameter | Measured | Tuned | Change (%) |
|---|---|---|---|
| $L_c$ | 0.0089 | 0.00449 | -49.5 |
| $r_{maj}$ | 0.105 | 0.0834 | -20.6 |
| $r_{min}$ | 0.105 | 0.12 | 14.7 |
| $T_{Tx}$ | 100 | 103 | 3.09 |
| $H_c$ | 0.0518 | 0.0504 | -2.88 |
| $L_{Rx2}$ | 0.0186 | 0.019 | 2.09 |
| $T_{Rx1}$ | 150 | 153 | 1.95 |
| $H_{Rx2}$ | 0.028 | 0.0276 | -1.56 |
| $V_{Rx2}$ | 0.033 | 0.0326 | -1.35 |
| $T_{Rx2}$ | 750 | 742 | -1.06 |
| $V_c$ | 0.0668 | 0.0662 | -0.903 |

on a Lenovo ThinkStation P520, with 128GB RAM. This is subject to change with coil parameters and model geometry studied, but provides a useful gauge for the relative speed up of a filament model.

Table 7: Filament Model Parameters

| Parameter | Measured | Tuned | Change (%) |
|---|---|---|---|
| $L_c$ | 0.0089 | 0.00507 | -43 |
| $T_{Tx}$ | 100 | 75 | -25 |
| $L_{Rx2}$ | 0.0186 | 0.0203 | 8.93 |
| $H_c$ | 0.0518 | 0.0485 | -6.49 |
| $T_{Rx1}$ | 150 | 142 | -5.29 |
| $r_{maj}$ | 0.105 | 0.11 | 5.23 |
| $V_c$ | 0.0668 | 0.0698 | 4.42 |
| $r_{min}$ | 0.105 | 0.103 | -1.56 |
| $V_{Rx2}$ | 0.033 | 0.0328 | -0.613 |
| $H_{Rx2}$ | 0.028 | 0.0281 | 0.377 |
| $T_{Rx2}$ | 750 | 753 | 0.339 |

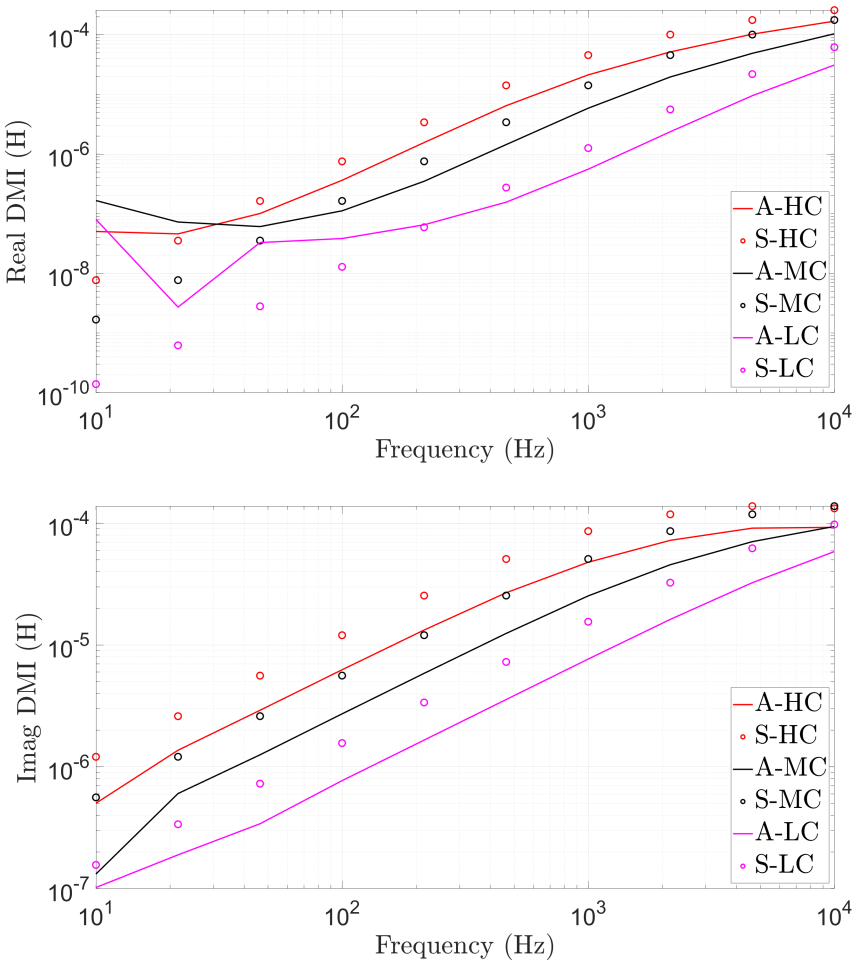


Figure 5: The simulated and actual measurement of the three calibration bricks, using the initial measured coil parameters in a 3D coil model. The prefixes A and S stand for actual and simulated, respectively

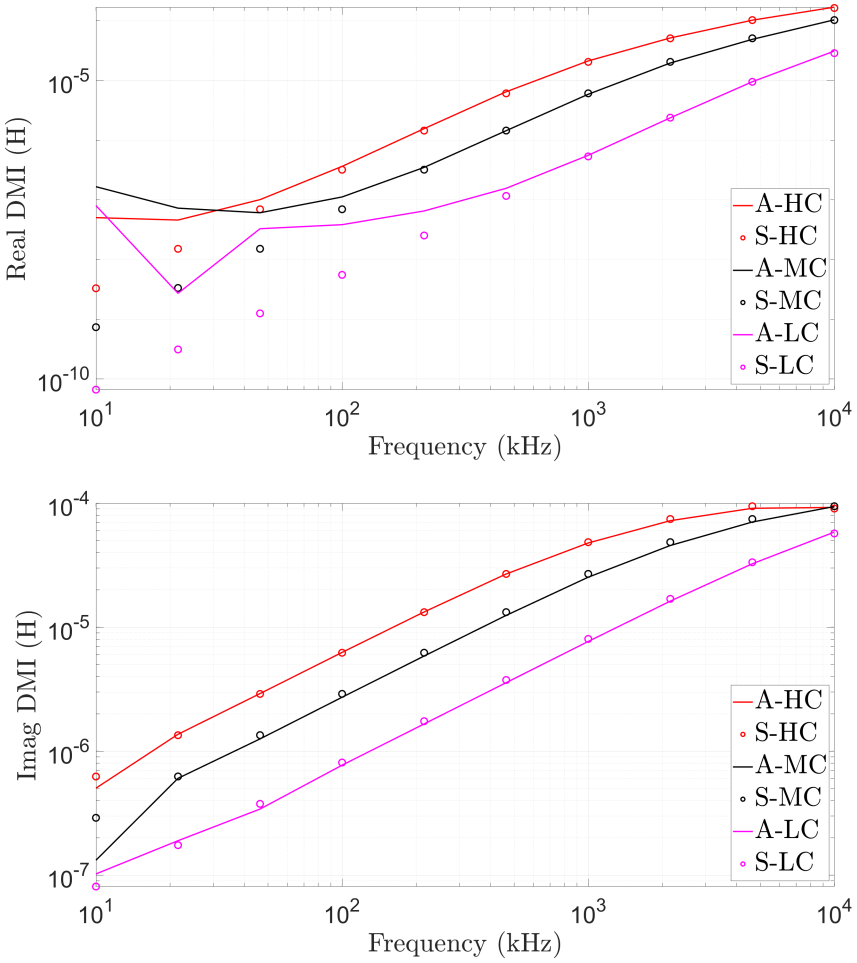


Figure 6: The simulated and actual measurement of the three calibration bricks, using a 3D coil model — post optimisation.

# 5 Conclusion

In this paper we have presented a method for tuning multiple coil parameters in order to calibrate a finite element model for use in an eddy current inspection application. The algorithm used is practical and requires no further theory beyond trust region algorithms; this algorithm can be used in both constrained and unconstrained optimisation. We have shown how the choice of finite element model can be determined through this calibration procedure. In this work we have shown that, in this particular nuclear graphite application and for the measurement device used, a filament model is as accurate as a 3D model for the sensor coils. Further, the calibration procedure used in this paper shows how to methodically reduce the error between finite element models and physical systems and is useful for applications such as the generation of synthetic training data for use in machine learning algorithms.

# Bibliography


[1] H. Tesfalem and A. J. Peyton and A. D. Fletcher and M. Brown and B. Chapman, "Conductivity Profiling of Graphite Moderator Bricks From Multifrequency Eddy Current Measurements," *IEEE Sensors Journal*, vol. 20, no. 9, 2020, pp 4840- 4849.

[2] B. Dekdouk and R. Chapman and M. Brown and A. J. Peyton, "Evaluating the conductivity distribution in isotropic polycrystalline graphite using spectroscopic eddy current technique for monitoring weight loss in advanced gas cooled reactors," *NDT and E International*, vol. 51, 2012, pp 150-159.

[3] M. Cheney and D. Isaacson and J. Newell and S. Simiske and J. Goble, "NOSER: An Algorithm for Solving the Inverse Conductivity Problem," *International Journal of Imaging Systems and Technology*, vol. 2, 1990, pp 66-75.

[4] N. G. Gencer and M. N. Tek, "Electrical Conductivity Imaging via Contactless Measurements," *IEEE Transactions on Medical Imaging*, vol. 18, no. 7, 1999, pp 617–627.

[5] T. J. Yorkey and J. G. Webster and W. J. Tompkins, "Comparing Reconstruction Algorithms for Electrical Impedance Tomography," *IEEE Transactions on Biomedical Engineering*, vol. BME-34, no. 11, 1987, pp 843 - 852.

[6] W. Yin and S.J. Dickinson and A.J. Peyton, "Imaging the Continuous Conductivity Profile Within Layered Metal Structures Using Inductance Spectroscopy," *IEEE Sensors Journal*, vol. 5, no. 2, 2005, pp 161 - 166.

[7] W. Yin and S.J. Dickinson and A.J. Peyton, "Evaluating the Permeability Distribution of a Layered Conductor by Inductance Spectroscopy," *IEEE Transactions on Magnetics*, vol. 42, no. 11, 2006, pp 3645-3651.

[8] V. Puzyrev, "Deep learning electromagnetic inversion with convolutional neural networks," *Geophysical Journal International*, vol. 218, no. 2, 2019, pp 817–832.

[9] H. Tesfalem; J. Hampton; A. D. Fletcher; M. Brown; A. J. Peyton, "Electrical Resistivity Reconstruction of Graphite Moderator Bricks From Multi-Frequency Measurements and Artificial Neural Networks," *IEEE Sensors Journal*, vol. 21, no. 15, 2021, pp 17005 - 17016.

[10] J. Hampton and H. Tesfalem and A. Fletcher and A. Peyton and M. Brown, "Reconstructing the Conductivity Profile of a Graphite Block using Inductance Spectroscopy with Data-Driven Techniques," *Insight-Non-Destructive Testing and Condition Monitoring*, vol. 63, no. 2, 2021, pp 82-87.

[11] G. Tian and A. Sophian, "Defect classification using a new feature for pulsed eddy current sensors," *NDT and E International*, vol. 38, no. 1, 2005, pp 77-82.

[12] A. Fletcher, "Non-Destructive Testing of the Graphite Core within an Advanced Gas-Cooled Reactor," PhD thesis, Dept. Electronic and Electrical Engineering, Univ. of Manchester, Manchester, United Kingdom, 2014.

[13] H. Tesfalem, "Eddy Current Based Non-Destructive Testing of the Advanced Gas-Cooled Reactor Core," PhD thesis, Dept. Electronic and Electrical Engineering, Univ. of Manchester, Manchester, United Kingdom, 2018.

[14] M.Fan, B. Cao, P.Yang, W. Lia and G. Tian, "Elimination of liftoff effect using a model-based method for eddy current characterization of a plate," *NDT and E International*, vol. 74, 2015, pp 66-71.

[15] J. Hampton and A. Fletcher and H. Tesfalem and A. Peyton and M. Brown, "A Comparison of Non-Linear Optimisation Algorithms for Recovering the Conductivity Depth Profile of an Electrically Conductive

Block Using Eddy Current Inspection," *NDT and E International*, Nov. 2021.

[16] A. Conn and M. Gould and P. Toint, "Global Convergence of the Basic Algorithm," in *Trust-Region Methods,* Society for Industrial and Applied Mathematics, 2000, pp. 115-168.

[17] G. A. F. Seber and C. J. Wild, "Computational Methods for Nonlinear Least Squares," in *Nonlinear Regression,* Wiley, 1989, pp. 619-660.

[18] J. Nocedal and S. J. Wright, "Trust-Region Methods," in *Numerical Optimization,* Springer, 2006, pp. 66-98.

[19] A. Conn and M. Gould and P. Toint, "The Trust-Region Subproblem," in *Trust-Region Methods,*Society for Industrial and Applied Mathematics, 2000, pp. 169-248.

[20] J. Nocedal and S. J. Wright, "Fundamentals of Algorithms for Nonlinear Constrained Optimization," in *Numerical Optimization,* Springer, 2006, pp. 421-446.

[21] J. S. Arora, "More on Numerical Methods for Constrained Optimum Design," in *Introduction to Optimum Design,* Academic Press, 2017, pp. 555-599.

[22] J. S. Arora, "Numerical Methods for Constrained Optimum Design," in *Introduction to Optimum Design,* Academic Press, 2017, pp. 511-553.

[23] R. Fletcher, "Introduction," in *Practical Methods of Optimization: Part 2 Constrained Optimisation,* Wiley, 2000, pp. 139 - 149 .

[24] H. Tesfalem and A. D. Fletcher and M. Brown and B. Chapman and A. J. Peyton, "Study of asymmetric gradiometer sensor configurations for eddy current based non-destructive testing in an industrial environment," *NDT and E International*, vol. 100, 2018, pp 1-10.

[25] H. Tesfalem and A. J. Peyton and A. D. Fletcher and M. Brown and B. Chapman, "Eddy Current Sensor and Inversion Technique for Estimation of the Electrical Conductivity Profile of the Graphite Bricks in an Advanced Gas-Cooled Reactor Core," *Studies in Applied Electromagnetics and Mechanics: Electromagnetic Non-Destructive Evaluation*, vol. 138, 2017, pp 253-264.

[26] T. Coleman and Y. Li, "An Interior Trust Region Approach for Nonlinear Minimization Subject to Bounds," *SIAM Journal on Optimization*, vol. 6, no. 2, 1996, pp 418–445.

[27] I. Miccoli, F. Edler, H. Pfnür and C. Tegenkamp, "The 100th anniversary of the four-point probe technique: the role of probe geometries in isotropic and anisotropic systems," *Journal of Physics: Condensed Matter*, vol. 27, 2015